OPEN ACCESS
IOP Publishing | International Atomic Energy Agency
Nuclear Fusion
Nucl. Fusion **56** (2016) 126001 (16pp)
doi:10.1088/0029-5515/56/12/126001

NTM stabilization by alternating O-point EC current drive using a high-power diplexer

W. Kasparek[1], N. Doelman[2,4], J. Stober[3], M. Maraschek[3], H. Zohm[3], F. Monaco[3], H. Eixenberger[3], W. Klop[2], D. Wagner[3], M. Schubert[3], H. Schütz[3], G. Grünwald[3], B. Plaum[1], R. Munk[1], K.H. Schlüter[1] and ASDEX Upgrade Team[3]

[1] Institut für Grenzflächenverfahrenstechnik und Plasmatechnologie, Universität Stuttgart, D-70569 Stuttgart, Germany
[2] Department of OptoMechatronics, TNO Technical Sciences, NL-2600 AD, Delft, The Netherlands
[3] Max-Planck-Institut für Plasmaphysik, 85748 Garching and 17491 Greifswald, Germany
[4] Leiden Observatory, Leiden University, NL-2333 CA, Leiden, The Netherlands

E-mail: walter.kasparek@igvp.uni-stuttgart.de

Received 20 May 2016, revised 15 July 2016
Accepted for publication 1 August 2016
Published 31 August 2016

Abstract

At the tokamak ASDEX Upgrade, experiments to stabilize neoclassical tearing modes (NTMs) by electron cyclotron (EC) heating and current drive in the O-points of the magnetic islands were performed. For the first time, injection into the O-points of the revolving islands was performed via a fast directional switch, which toggled the EC power between two launchers synchronously to the island rotation. The switching was performed by a resonant diplexer employing a sharp resonance in the transfer function, and a small frequency modulation of the feeding gyrotron around the slope of the resonance. Thus, toggling of the power between the two outputs of the diplexer connected to two articulating launchers was possible. Phasing and control of the modulation were performed via a set of Mirnov coils and appropriate signal processing. In the paper, technological issues, the design of the diplexer, the tracking of the diplexer resonance to the gyrotron frequency, the generation and processing of control signals for the gyrotron, and the typical performance concerning switching contrast and efficiency are discussed. The plasma scenario is described, and plasma experiments are presented, where the launchers scanned the region of the resonant surface continuously and also where the launchers were at a fixed position near to the $q = 1.5$-surface. In the second case, complete stabilization of a 3/2 NTM could be reached. These experiments are also seen as a technical demonstration for the applicability of diplexers in large-scale ECRH systems.

Keywords: NTM stabilization, fast switching of EC power, high-power diplexers, electron cyclotron heating and current drive

(Some figures may appear in colour only in the online journal)

1. Introduction: NTM stabilization, techniques

Neoclassical tearing modes (NTMs) are magneto-hydrodynamic (MHD) instabilities, which can be excited in high-beta tokamak plasmas. They are characterized by magnetic islands located on rational magnetic surfaces, which typically rotate with the plasma around the tokamak axis. NTMs significantly increase the radial transport, and thus reduce the performance of fusion plasmas [1].

Electron cyclotron resonant heating (ECRH) and electron cyclotron current drive (ECCD) with high-power millimeter waves can stabilize NTMs, if the power deposition is aligned with the mode location [2, 3, 4, 5]. For ITER, the suppression of NTMs is a main purpose of ECCD applied from the upper

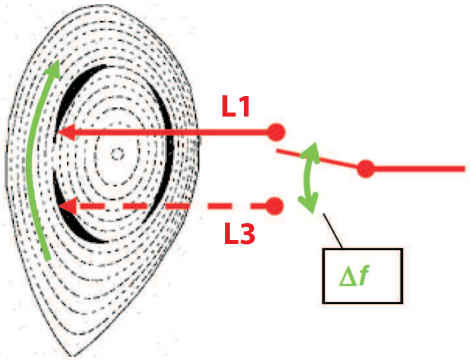

Figure 1. Sketch of the NTM structure in a tokamak, and the principle of the synchronous stabilization of NTMs using a fast directional switch.

launchers [6]. Depending on the beam divergence, mode purity, and mutual misalignment of the launchers, as well as beam broadening by turbulence, the width of the power deposition profile w_{CD} can exceed the marginal width of the island w_{marg} for stabilization [7, 8]. For this case, the highest efficiency for NTM stabilization is reached when ECCD is applied in the center (the O-point) of the island; ECCD between the islands (in the X-points) may even destabilize the modes. Therefore, modulated injection of the launched power synchronous with the frequency of the rotating islands may be required [1].

Up to now, synchronous current drive has been performed by power modulation of the gyrotron [2], with the disadvantage that some of the installed power is wasted with the amount dependent on the ratio w_{CD}/w_{marg}. An alternative for power modulation could be the synchronous toggling of the gyrotron power between two launchers directing the beam to poloidal or toroidal planes, which are about $(2\,k+1)\,^{*}\,180°$ away from each other with respect to the phase of the NTM, as sketched in figure 1. Here, k is an integer with $k \geqslant 0$. (Alternatively, the power of one output can be used for synchronous NTM stabilization, while the other output feeds a launcher for an independent ECRH or ECCD experiment.)

The (non-mechanical, electronically controlled) switching can be performed with a resonant diplexer [9, 10], which is operated as a fast directional switch (FADIS), while the gyrotron source operates continuously.

The FADIS operation is based on the transmission characteristics of a resonant diplexer. This device consists basically of a ring resonator made of two focusing mirrors and two plane coupling gratings, as sketched in figure 2, left. The resulting transmission functions are narrow resonances at output 2 (the 'resonant channel'), which are periodic with c/L, and broad transmission regions with notches in between at output 1 (the 'non-resonant channel'), shown in figure 2, right. The width of the resonances is determined by the diffraction efficiency R_1 of the coupling gratings. With control of the resonator length L by making one of the resonator mirrors movable, the diplexer can be tuned with respect to the gyrotron frequency f_{gyr} according to the application. In particular, it can be tuned to point B by having f_{gyr} and L correspond to the slope of the resonance (tracking to the slope). For the toggling of the power between the diplexer outputs, a small frequency-shift keying of the gyrotron between two frequencies f_1 and f_2 corresponding to the upper and lower frequencies of the slope of the resonance is needed (figure 2, right). This is performed by modulation of the gun anode or the beam acceleration voltage of the gyrotrons. Note that this voltage modulation usually causes a reduction of power during the low-voltage phase. Note also that for the tiny frequency shifts of some tens of megahertz needed for the switching, no remarkable change in the deposition radius in the plasma occurs.

In this paper, experiments to stabilize NTMs on ASDEX Upgrade by fast switching between two launchers are described. Note that synchronously power-modulated NTM stabilization experiments have been performed at ASDEX Upgrade [2] and other tokamaks like DIII-D [5] and JT60-U [3]. The main motivation of the work is the demonstration of the applicability of resonant diplexers for NTM stabilization. The paper is organized as follows: in section 3, we revisit the case of modulated O-point current drive without switching. In section 4, technical issues related to fast switching are addressed, such as the FADIS setup and the control of its resonator. Section 5 describes the NTM stabilization experiments using fast switching. Finally, conclusions are given in view of the application of the diplexer technology to large ECRH systems.

2. NTM stabilization with modulated ECCD—test case without FADIS

Before studying the effect of fast switching between L1 and L3 as sketched in figure 1, we address the case of using only one launcher with maximum power modulation in phase with a fast rotating NTM. The basic concept for NTM stabilization is to maximize the power when the absorption location is close to the O-point of the island and to minimize the power when it is close to the X-point. Note that current driven outside the island can even have a destabilizing effect. The concept has been first experimentally demonstrated on ASDEX Upgrade [2]. It may even become a necessary condition for complete stabilization in cases when the ECCD deposition width is significantly greater than the marginal island width, below which the island becomes unstable and vanishes on its own.

As a reference for the fast switching experiment we first have reestablished NTM stabilization with a modulated ECCD beam using one launcher. First we discuss the somewhat different absorption geometry (as compared to [2]), then we address diagnostic and technical issues related to NTM-phase-locked gyrotron modulation and finally we show the stabilization results for different phase angles and continuous wave (cw) operations.

2.1. Plasma scenario

Figure 3 compares several possible settings of an AUG ECRH launcher to drive localized plasma current. Experiments in [2] used a high-field-side resonance with absorption close to the plasma mid-plane (black curves in the middle part of the figure, corresponding to toroidal launching angles of 5°, 15°

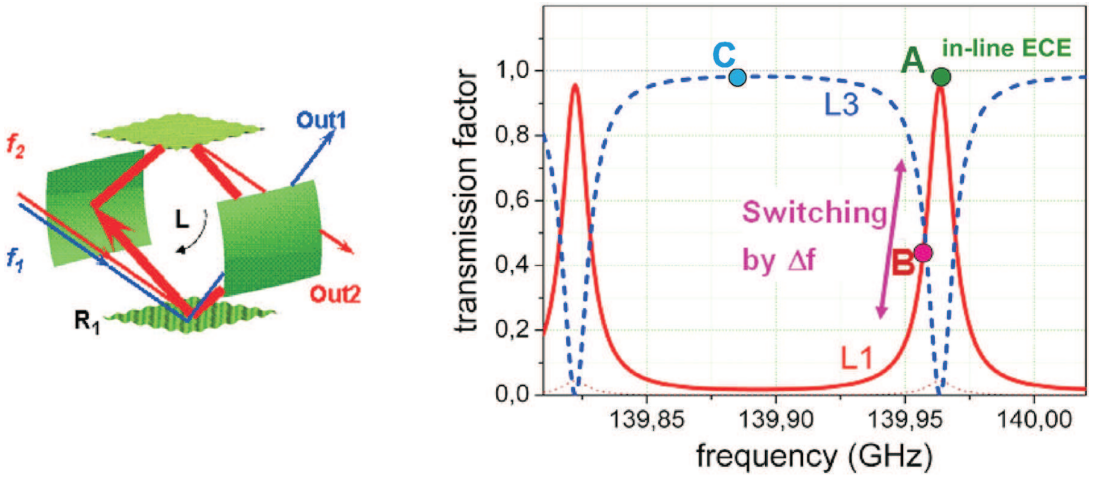

Figure 2. Left: principle of a ring resonator diplexer. Right: transmission functions for the resonant (OUT2, red, solid) and the non-resonant (OUT1, blue, dashed) output, calculated for the parameters of the diplexer Mk IIa with a resonator length of $L = 2.121$ m, and a grating coupling efficiency of $R_1 = 0.22$. The pink dot shows the operation point B for fast switching generated by a small frequency modulation.

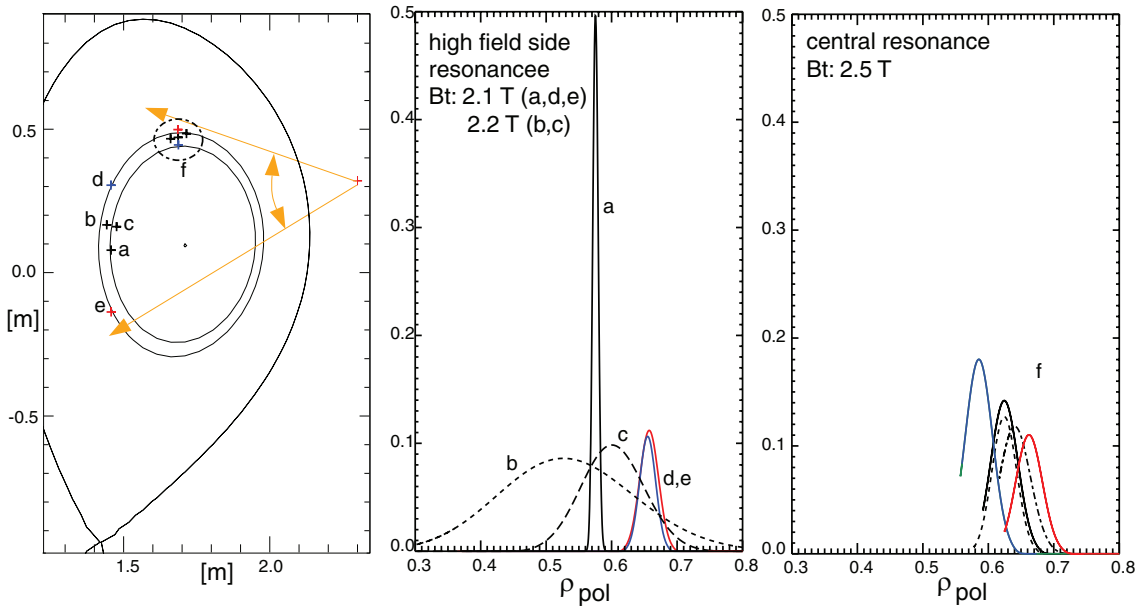

Figure 3. Beam tracing results for different values of toroidal field B_t and launching angles. Kinetic and (scaled) magnetic data from discharge 24061 at 3.5 s. Left: position of the maxima of j_{ECCD} for the various cases, projected on a poloidal cross section of the torus, together with a sketch of the launching geometry. The radial position of the maxima depends on the value of B_t. Middle: $j_{ECCD}(\rho)$ (MA $(m^2MW)^{-1}$) for the resonance located on the high-field side ($B_t = 2.1$–2.2 T). The solid curves correspond to a 5° toroidal angle at 2.1 T, and the dashed curves correspond to 15° and 20° at 2.2 T. Right: $j_{ECCD}(\rho)$ for the resonance through the plasma center ($B_t = 2.5$ T). The solid curves correspond to a 15° toroidal angle, and the dashed curves correspond to 10° and 20°.

and 20°). Larger toroidal launching angles lead at this location to wide ECCD profiles, whereas small toroidal angles lead to high but narrow current density profiles. These profiles are a consequence of the resonance surface being almost identical to a flux surface in the absorption region. The properties of this setup were ideal for the studies presented in [2]. It was shown that the widening of a cw-beam by increasing the toroidal launching angle hampered the full stabilization of the NTM, which could be regained using O-point modulation (roughly 50% duty cycle). X-point modulation was less stabilizing (in terms of the minimum achieved mode-amplitude) than cw.

Since 2007 AUG has been operated with *W*-coated plasma-facing components. As a consequence, central wave heating is required for the stable operation of H-mode plasmas with significant β [11]. The plasmas in [2], which did not use central wave heating, could not be reproduced yet. In order to provide central ECRH at the same time when tackling NTM stabilization, the cold resonance has to be close to the magnetic axis. Recent experiments on feedback-controlled NTM

stabilization [12] have therefore focused on such a configuration leading to ECCD profiles as in the right part of figure 3. Here, the resonance cylinder is almost perpendicular to the flux surface such that the deposition width (in ρ) is determined by the beam width, and it does not depend significantly on the toroidal angle (between 10° and 20°). The driven current density j_{ECCD} is lower compared to the high-field-side resonance when depositing at the mid-plane, but it is not significantly different from an HFS deposition above or below the mid-plane. The latter positions have to be chosen for feedback control with a movable launcher, since the position at the mid-plane does not allow one to shift the deposition towards lower ρ. In this sense, the new configuration has no significant drawback for NTM stabilization using a movable mirror as actuator.

Unfortunately, this new configuration does not allow one to repeat experiments with wide deposition and modulated ECCD as shown in [2]. With a narrow deposition, the beneficial effect of O-point modulation is known to be smaller than for a wide beam [8]. From figure 3, one can estimate the width of the ECCD beams to be $w_{\mathrm{CD}} = 3$ cm. The typical width of the marginal island could not be measured at $B_{\mathrm{t}} = 2.4$ T, as the ECE system is not optimized for this case. From a correlation and phase analysis [13] of the ECE signals of similar discharges at $B_{\mathrm{t}} = 2.6$ T, a typical island width of $w = 7$ cm is obtained [12], and the resulting estimate for the marginal island size is $w_{\mathrm{marg}} = 5$ cm. As these values are not very precise, we therefore compare the effect of NTM-modulated ECCD centered either on the O-point or on the X-point of the island with cw ECCD in a first step. For this purpose we want to use only one ECCD beam (later we have only one FADIS), and, therefore, we reduce the heating significantly after having created the NTM in order to reduce its strength and to facilitate stabilization. In [11] it is described that the central ECRH preventing W accumulation (provided by other gyrotrons) should be deposited within $\rho_{\mathrm{pol}} < 0.2$. Using 140 GHz and taking into account the Shafranov shift of the plasma center, this boundary condition on ρ limits the toroidal field in the geometric center of the vessel between $2.4\ \mathrm{T} < B_{\mathrm{t}} < 2.65$ T. As described in section 2.2, the lower value had to be chosen. It requires large toroidal angles ($\pm 20°$) for the central heating beams such that the Doppler shift moves the absorption region towards larger major radii and inside the $\rho = 0.2$ surface. For this purpose, two ECRH beams with opposite toroidal angles were used in order to cancel the current drive effects. The equilibrium with the locations of absorption is shown in figure 8 (left part) for the FADIS configuration. For the results presented in the section below, only launcher L3 is used (no FADIS operation).

2.2. NTM location, Mirnov coil signals

The concept of how to lock the ECCD modulation to a certain phase of the toroidally rotating NTM has already been described in [2] and in more detail in [4]. As a fingerprint for an (m,n)-NTM, specific Mirnov coil signals are analogly combined. In the papers cited above, signals specific to even or odd n-numbers were generated. Meanwhile the concept is more sophisticated allowing one to also separate even and odd m numbers. For the (3,2)-NTMs tackled in the experiments described here we therefore use the even-n, odd-m signal as a reference for the NTMs.

As already discussed in [2, 4], there is an intrinsic phase delay between the Mirnov signal and the ECCD modulation due to two independent effects. The O-point corresponds to the zero of $\dot{B}_R$ where the sign of $\dot{B}_R$ changes from positive to negative, resulting in a phase difference of 90° between the maximum of $\dot{B}$ and the center of the ECRH on the interval. An additional phase difference arises when taking account of the different locations of ECCD and $\dot{B}$ measurement on the flux surface as discussed in detail in the abovementioned references. Adding the two phases with the correct signs results in a phase difference, which has to be technically realized with the gyrotron as will be described in the next section.

As described in the introduction for the fast switching experiment, NTM amplitudes should be $\approx 180°$ out of phase at the absorption locations for the two launchers in order to allow 'continuous' O-point heating. This additional requirement determines the choice of B_{t}. The best choice within the range of $2.4\ \mathrm{T} < B_{\mathrm{t}} < 2.65$ T necessary for sufficient central heating (see above) is at 2.4 T. Figure 4 illustrates the situation. The phase of the mode is plotted as a function of the poloidal and toroidal angles on the $q_{95} = 1.5$ surface allowing a direct comparison of the relative phases at the location of the Mirnov coils and the locations of absorption of the two launchers. This allows one to obtain a request for the ideal relative phasing of the (50% duty cycle) power modulation of the launchers with respect to the Mirnov signal. In the next section we will describe how and how well this has been realized. Note that the ideal phase delay between the two launchers is close to 180°, i.e. well suited for the switching experiment. For the experiments without a FADIS, described in section 2.4, we only used L3. The estimated relative phasings as shown in figure 4, bottom, depend somewhat on the equilibrium used, resulting in an error of the relative phasing of $\approx \pm 10°$.

2.3. From Mirnov signals to gyrotron control

On AUG, Mirnov signals generated by rotating (3,2)-NTMs span a frequency range between 10 kHz and 25 kHz. One period is therefore ≈40–100 μs. An accuracy of 1 μs is required for the power switching to achieve a phase match better than 10°. The time for Mirnov data acquisition, analog linear combination and transmission via 100 m of optical fiber is estimated to be faster than 100 ns. The latter step consists of a voltage–frequency converter (10 MHz ± 1 MHz corresponds to ±10 V). The frequency is transmitted through the glass fiber by light flashes and back-converted to a voltage on the other side. A transmission time below 100 ns has been explicitly verified using two independent data loggers on both ends of the optical fiber (analog input versus analog output), both triggered by the optical-fiber based AUG trigger system. These small time-shifts are neglected in the following. An analog phase shifter converts the Mirnov signal into phase-shifted trigger-pulses for the series-tube modulator. During the low period of the

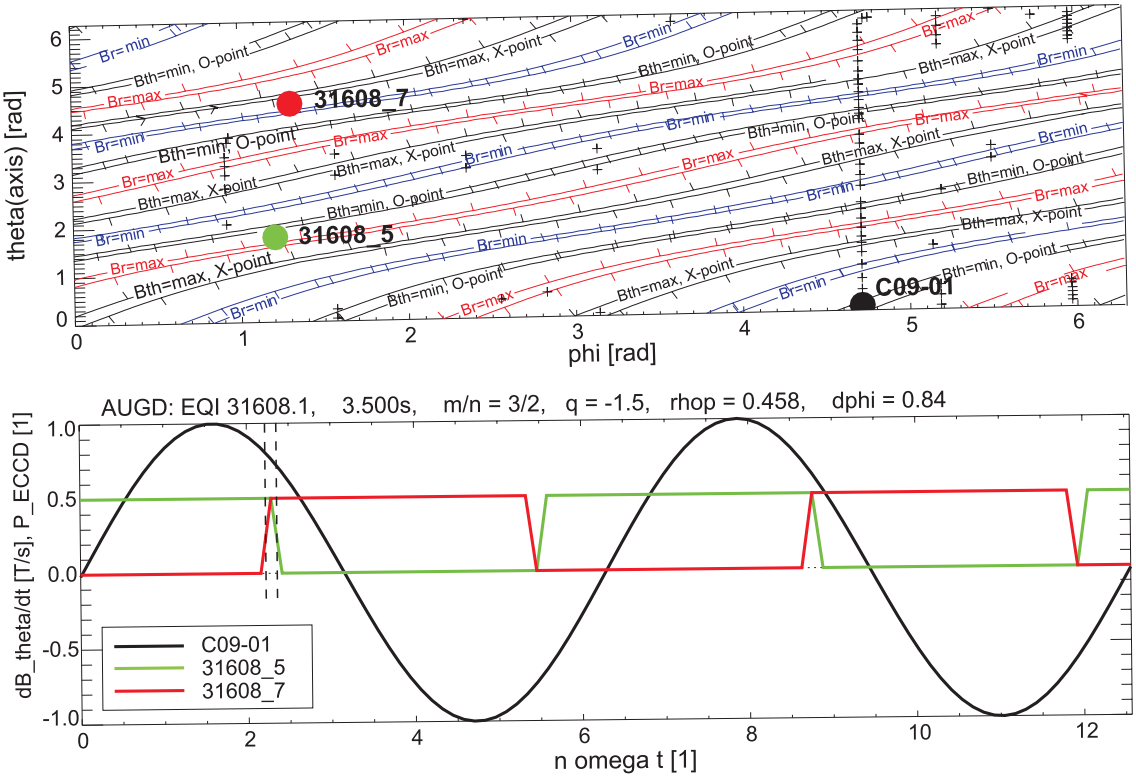

Figure 4. Top: phase of the (3,2) NTM on the $q_{95} = 1.5$ surface as a function of the toroidal and poloidal angles in radians. The zero of the poloidal angle is at the outer mid-plane. Small crosses indicate the position of the Mirnov coils. The three colored dots correspond to the positions of the reference Mirnov coil (black), launcher L1 (green), and launcher L3 (red). Bottom: ideal relative time traces for maximum O-point heating for 50% duty cycle and independent ECRH beams for $\dot{B}$ and the power across the respective launchers L1 (green) and L3 (red), for $B_t = 2.4$ T.

trigger the modulator reduces the acceleration voltage of the electron beam in the gyrotron by a pre-set value. In the case shown here from −41.5 kV to −28.5 kV (constant depression +32 kV) a reduction of the power from 700 kW to 130 kW has resulted. Data transmission to the series modulator uses a digital optical transmission which introduces a fixed delay of 18 μs. This results in an uncomfortable procedure to achieve the requested phase delay between the Mirnov signal and ECCD: based on the expected frequency of the mode, the 18 μs is converted into a phase difference which is subtracted from the requested phase difference. The result is then set at the phase shifter with the help of a function generator and an oscilloscope. Additionally, the trigger level has to be set at the phase shifter in order to prevent triggering on noise without losing too much sensitivity on real modes. If the real frequency differs from the expected frequency this leads to an improper phasing as further discussed in section 2.4. In principle such problems could be avoided by inclusion of the fixed delay of 18 μs into an FPGA-based phase shifter if such operational scenarios will be requested more frequently. Figure 5 illustrates some of these issues. At the top left, an overview of the whole discharge is shown. The stabilization of an NTM is seen in the upper time trace. As the NTM is stabilized, the amplitude becomes so small that the locking is lost. The box average of the gyrotron power shows that during modulation the duty cycle is ≈50% changing to almost 100% as noise creates only occasional triggers[5]. Further insight into triggering requires a strong zoom (bottom left). At this zoom level it can be seen how other MHD disturbances (ELMs herein) affect triggering. They can suppress zero crossings due to the NTM oscillation, thereby blinding phase detection for some periods resulting in a loss of ≈2% of the NTM oscillations for these specific conditions. A further zoom allows one to check the phase shifts. As mentioned above, the shift between the top (green) and middle (red) curves can be adjusted at the phase shifter, but the time shift between the middle and lower curves is fixed (18 μs).

2.4. Variation of the phase angle

Figure 6 shows the reaction of a (3,2)-NTM to ECCD locked to the O-point, ECCD locked to the X-point, and with cw-ECCD. In the $I_p = 1$ MA, $B_t = -2.4$ T discharge, a (3,2)-NTM is triggered by a fast increase of the NBI-heating to 12.5 MW. The

[5] The reason for having 'full power' as a default lies in the technical realization of fast high-power modulation. The input power to the series modulator does not vary, but all power which is not output to the gyrotron during modulation is cooled away via the modulator anode. The default 'full power' therefore protects the tetrode, since it minimizes the heat load on its anode. In principle the discharge control system (DCS) could request to fully switch off the gyrotron (i.e. to apply a blocking voltage to the tetrode control grids) after it has detected a stabilization of the mode, but this has not yet been attempted.

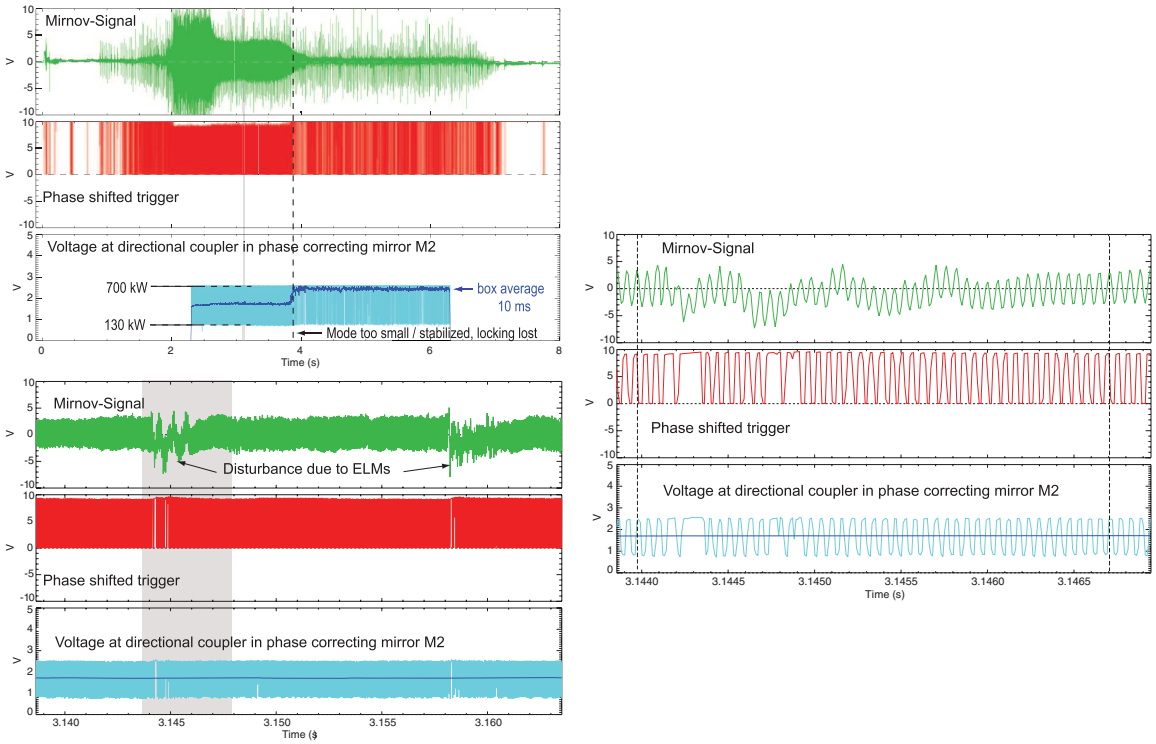

Figure 5. Time traces related to the mode-locked injection of ECCD (AUG discharge #29917 in figure 6). Middle: zoom into the top traces (×240). Zoomed time interval shaded in gray in top part. Bottom: zoom into the middle traces (×6); the zoomed interval is shaded in the middle part. The dashed vertical lines are added to see the phase differences at two arbitrary time points. Each of the three zoom-states consists of three time traces. Top (green): $\dot{B}$ from Mirnov coils linearly combined to correspond to odd m, even n. Middle (red): output of the phase shifting unit. Bottom (cyan, blue): voltage at the directional coupler embedded in the second matching mirror M2 of the matching-optics unit. Blue indicates the sliding box average over 10 ms.

ECCD deposition is twice scanned across the resonant surface by a pre-programmed rotation sequence for one launcher axis. For cw-operation and dominant O-point heating the mode disappears during the first crossing, roughly at the ρ-value expected from RT-Torbeam [14] and the estimated position of the (3,2)-surface [15]. For the O-point case, one of the underlying centrally-heating cw-gyrotrons is lost at ≈3.5 s, but the off-axis modulation works as planned. With dominant X-point heating the mode is not fully stabilized. In the latter case, the mode amplitude has two minima in the vicinity of the two expected crossings. The cw-power is 700 kW, and the time-averaged power for O-point modulation is 410 kW.

We did not further study the minimum power for complete stabilization with cw and O-point modulation. Since CW can be regarded as a mixture of X- and O-point modulation it seems likely that the threshold for the time-averaged power should be somewhat lower for the O-point modulation. After stabilization of the NTM in the O-point and cw-case the stored energy recovers somewhat. Note that the NBI heating in this phase of the discharges has been reduced to 7.5 MW such that a full recovery of the maximum stored energy cannot be expected.

The power needed for these reference scenarios is not in line with the estimates given before: $w_{CD} = 3$ cm, $w_{marg} = 5$ cm. As the beneficial effect of O-point modulation is significant, we have to assume a ratio $w_{CD}/w_{marg} > 1$. The reason for this is not clear. Nevertheless, we have to take these reference values as the basis for comparison of the stabilization experiments for the diplexer discussed in chapter 4.

We end this section by discussing how well we did in matching the required modulation pattern (phasing of power on/off) compared to the ideal case shown in figure 4, the red and black curves in the bottom part. In the left part of figure 7, another pair of black and red curves is shown from the case we labeled O-point heating. Black is the Mirnov signal, and red the gyrotron power measured by a directional coupler. The comparison is not straightforward since the latter is sampled only with 100 kHz. We have concluded that the time jitter and averaging effects of the data acquisition systems are irrelevant here by using the 100 kHz system to measure the Mirnov data independently, and the data lie sufficiently well on the black curve. A simple analysis of the red curve in figure 7 can only locate the jump in power within ±5 μs since the coupler voltage typically changes in two steps (ΔU_1, ΔU_2) as sketched in the figure. More information can be gained by making a histogram over more than 20 000 switching cycles, binning $|\Delta U_2| - |\Delta U_1|$ by voltage steps of 10 mV. The result is shown in the top right part of figure 7. The two colors correspond to the rising and falling edges. The 'ears' at both sides indicate that the switching process is shorter than

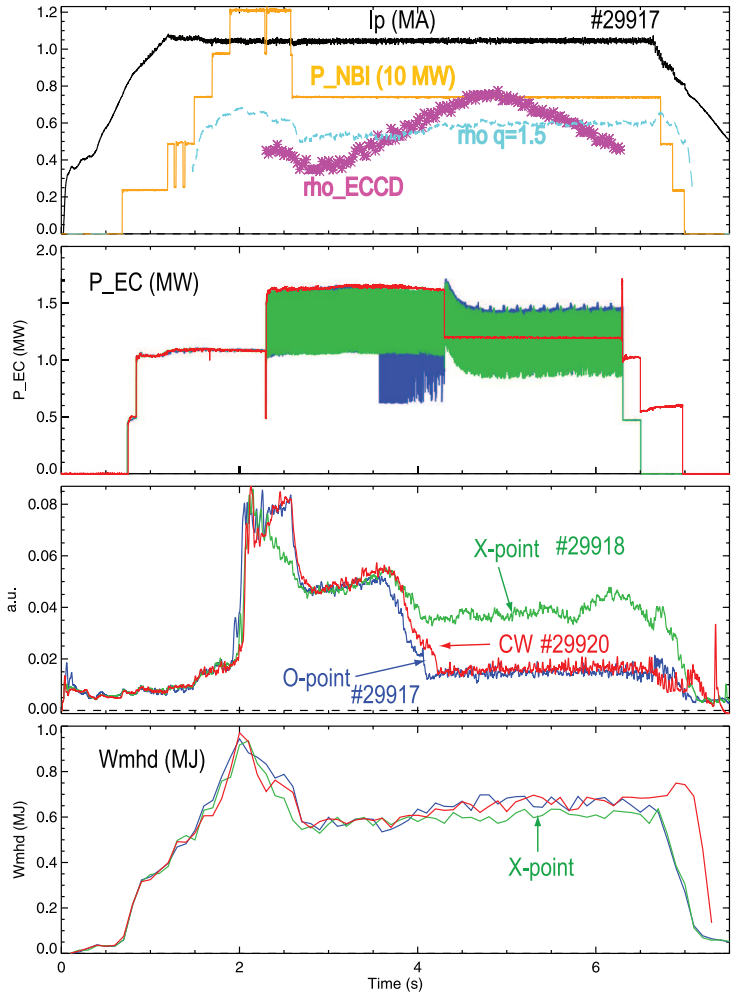

Figure 6. Comparison of three discharges with identical control parameters, except the modulation scheme. The latter was a 50% duty cycle close to the O-point (#29917), a 50% duty cycle close to the X-point (#29918) and a 100% duty cycle, i.e. cw (#29920). The upper box shows the scenario (all time traces in this box are from #29917 as a typical example): 'rho $q = 1.5$' corresponds to the ρ_{pol} value of the $q = 1.5$ surface as estimated from the real-time equilibrium. 'rho_ECCD' gives the location of the maximum ECCD as determined by RT-TORBEAM. The box second from the top shows the EC power. The color code is as indicated in the box below. The box second from the bottom shows the upper envelopes of the $\dot{B}$ signals of the Mirnov coils. Note that the noise level for these signals lies between 0.1 and 0.2 (a.u.), i.e. full stabilization is seen for $t > 4$ s in the O-point and cw cases. At the bottom the stored energy is shown. Same color code as above.

10 μs, but not much shorter; otherwise they should be more pronounced. Quantitative insight is gained by integration of the histogram and normalizing the maximum to unity as shown in the bottom right part. The curves can be regarded as probability distributions, i.e. they give the probability that for an average jump $|\Delta U_2|-|\Delta U_1|$ is larger than the respective abscissa value. Let us further assume that (a) all rising jumps (and independently all falling jumps) are physically sufficiently equal, (b) the jumps are symmetrical such that half of the jump amplitude is reached after half the jump time, and (c) the over 20 000 jumps cover stochastically the possible time deviation of ± 10 μs between the 'real' jump and the time when the intermediate data point (between ΔU_1 and ΔU_2) is sampled. Then the normalized integrals can be interpreted as calibration curves for the exact timing of the center of the jump as indicated by the additional labeling of the vertical axis. Obviously uncertainty rises as the center of the jump is more distant than ± 3.5 μs from the intermediate data point, indicating that the total jump duration is about 7 μs long. Also taking into account the asymmetry of this calibration curve with respect to the (0 V, 0 μs) point (which violates our initial assumption on the jump symmetry) we conclude that we can reconstruct the center-of-jump time with an uncertainty of ≈ 1 μs, depending on its closeness to the central data point. The vertical green (orange) dashed lines in the left part of figure 7 correspond to such reconstructed half-jump times for the rising (falling) edge of the power signal for four consecutive cycles. The phasing with respect to the Mirnov signal is stable within ± 2 μs. The power signal lags behind the Mirnov signal by about $100^\circ \pm 10^\circ$.

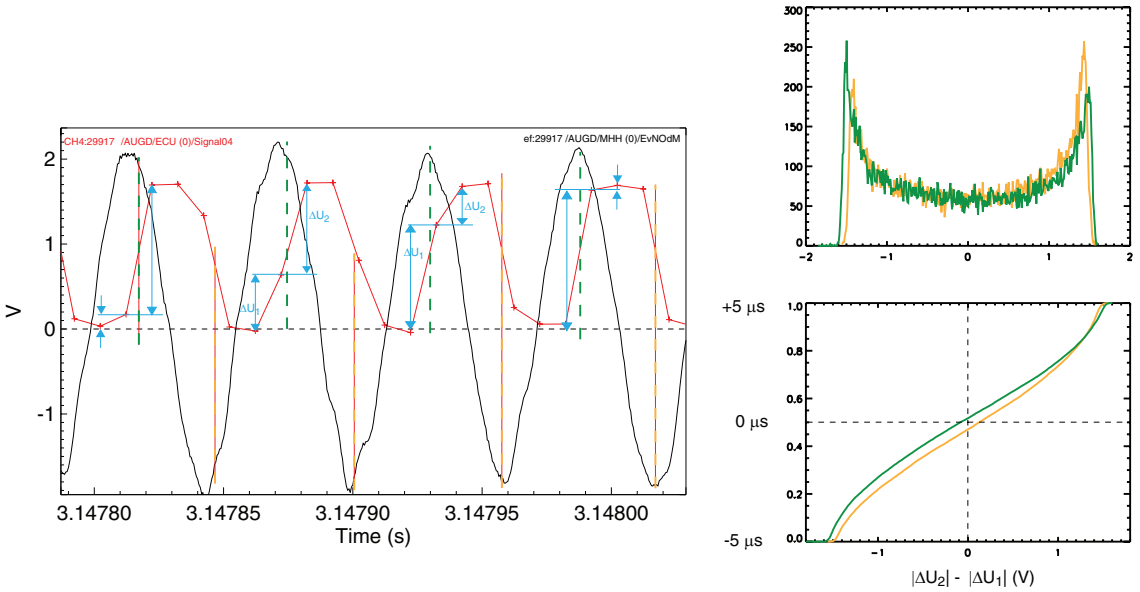

Figure 7. Left: Mirnov signal (black) and uncalibrated power signal (red) for the case of nominal O-point modulation (#29917). The straight lines are explained in the text. Right top: histogram of $|\Delta U_2|-|\Delta U_1|$ for the rising edges (green) and falling edges (orange) of the power signal. Sampled is the time interval (2.0 s, 3.8 s) with 26 000 jumps in each direction using a bin-width of 10 mV. Right bottom: normalized integrals of the curves on top.

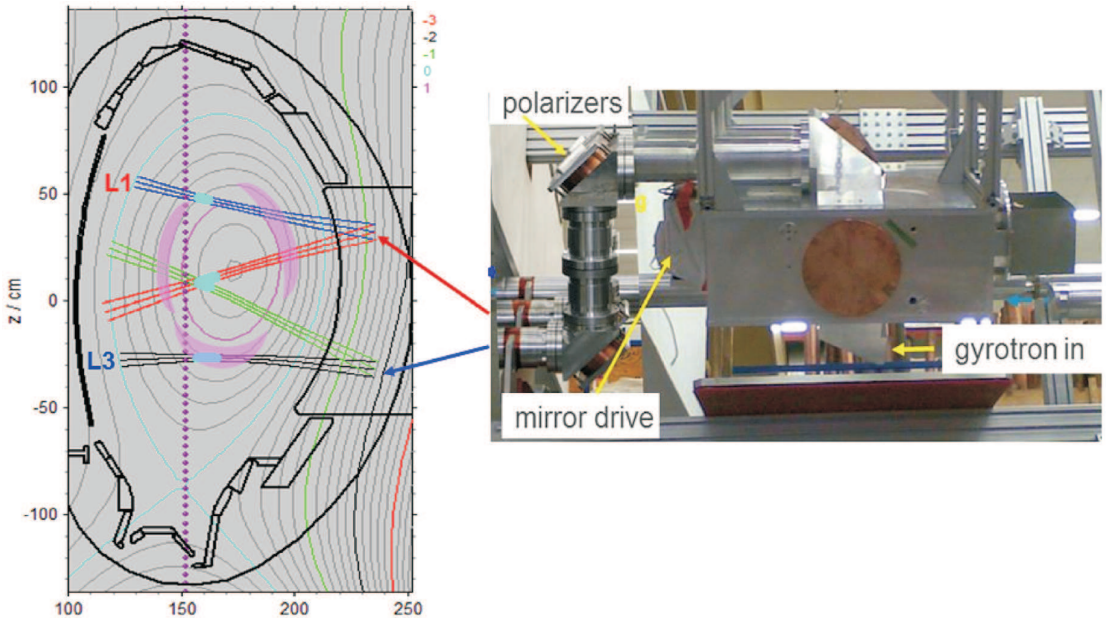

Figure 8. Left: cross-section of ASDEX Upgrade showing the typical setting of the antenna beams of the ECRH-2 system, and a sketch of the NTM structure. Right: photograph of the diplexer MK II installed in the ECRH-2 system at ASDEX Upgrade.

In figure 4, the optimum phase delay for O-point heating with L3 is close to 135°, so we were about 35° off the optimum. The reason for this mismatch is that the phase shifter setting was optimized for a mode frequency of 22 kHz, but the real frequency finally was 16 kHz, since we decided during the experiments to use one NBI source fewer in order to facilitate mode stabilization. As explained in section 2.3, such a frequency change would have required readjusting the phase delay between the Mirnov signal and gyrotron trigger. This was not attempted in this discharge. Fortunately, the mismatch is small enough such that there is still a significant contrast between our 'O-point' and 'X-point' modulation setups.

3. Diplexer technology, operation and control

3.1. Diplexer technology, FADIS operation

For experiments on NTM stabilization via synchronous switching between two launchers, the diplexer Mk II [10] was

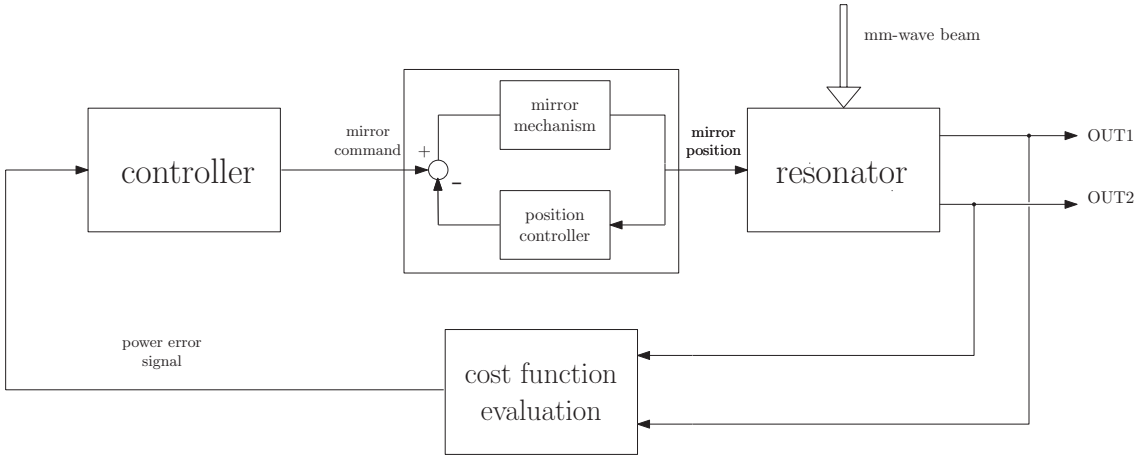

Figure 9. Block diagram of the resonator feedback control system, with mirror position feedback (inner loop) and OUT1 and OUT2 beam power feedback (outer loop).

used. Its functionality had been tested extensively before at the ECRH test stand at W7-X [16]. For experiments on ASDEX Upgrade, it was integrated into the HE_{11} corrugated waveguide transmission of the ECRH-2 system [17]. This system features four 140/105 GHz gyrotrons and four launchers, where the toroidal and poloidal injection angles can be controlled independently. The gyrotron Gy3 was connected to the input of the diplexer; the non-resonant output OUT1 was the feeding launcher L3, and the resonant output OUT2 was connected to launcher L1 (figure 8; see figure 2). To match the polarization to the launching geometry, miter-bend polarizers were installed behind the diplexer. (Note that the present diplexer operates with linear polarisation only.) The signals from the directional couplers installed in the transmission lines near to the launchers were used as input for the control of the resonator mirror drive; the controller was set for frequency tracking to operation point B on the positive (low-frequency) slope of the resonance.

3.2. Resonator control

The diplexer's transmission behavior strongly depends on the relation between the resonator round-trip length and the gyrotron frequency. As discussed in section 2, for fast switching the transmission behavior should correspond to point B of the transmission curves, as indicated in figure 2. By making one of the resonator's mirrors movable, the diplexer can be tuned to this operational point for a given gyrotron frequency f_{gyr}. Ideally, tuning of the diplexer would be an *a priori* calibration action, but in practice disturbances drive the diplexer out of this operational point. These disturbances are mainly due to:

1. Expansion of the cavity due to a temperature gradient.
2. Non-stationarity of the gyrotron center frequency f_{gyr}.
3. Structural vibrations acting on the resonator cavity—for instance, those induced by cooling pumps.

Therefore, in order to tune the resonator to its desired functionality and to reject external disturbances, the position of the movable resonator mirror needs to be controlled in real time. For this purpose a dedicated, mirror drive mechanism has been realized. It consists of a voice-coil actuator to move the mirror and an elastically deformable parallel leaf spring mechanism to guide the mirror. This type of guiding is friction-free. The leaf spring mechanism has high stiffness in five degrees of freedom of the mirror, whereas it is compliant for motion in the desired direction. To enable control of the position of the mirror relative to its casing a position sensor has been added. This optical encoder measures the displacement of the mirror base relative to the frame with a resolution of 0.1 μm. More details of this mirror drive mechanism can be found in [18].

The encoder signal from the position sensor is being used in an inner feedback control loop to enhance the bandwidth of the mirror motion system. This position controller has been tuned on the basis of loop-shaping techniques. By doing so, the bandwidth of the mirror motion system has been increased from 8 Hz in an open loop to approximately 100 Hz in a closed loop. For the fast switching functionality of the diplexer, its desired set-point will be halfway the slope of both transmission curves, similar to point B as shown in figure 2. The inner position control loop is not suitable for tuning the resonator to this set-point, since this would require an accurate model of the resonator and exact knowledge of the gyrotron frequency together with an absolute calibration of the movable mirror position. It would be much more direct to use the actual power values of the output beams OUT1 and OUT2 in a control loop, since these variables directly characterize the resonator behavior. Moreover, output power feedback will render the necessary absolute positioning accuracy to the mirror motion system.

A suitable error function e for the feedback control loop is the difference between the power of both output beams OUT1 and OUT2, represented by $e = \text{OUT1} - \text{OUT2}$. Then, for the fast switching function the controller ideally tunes the resonator by driving the error signal e to zero. The block-diagram of this output beam power feedback system is shown in figure 9.

Designing a controller for output power-based feedback is not as straightforward as for mirror position feedback. In

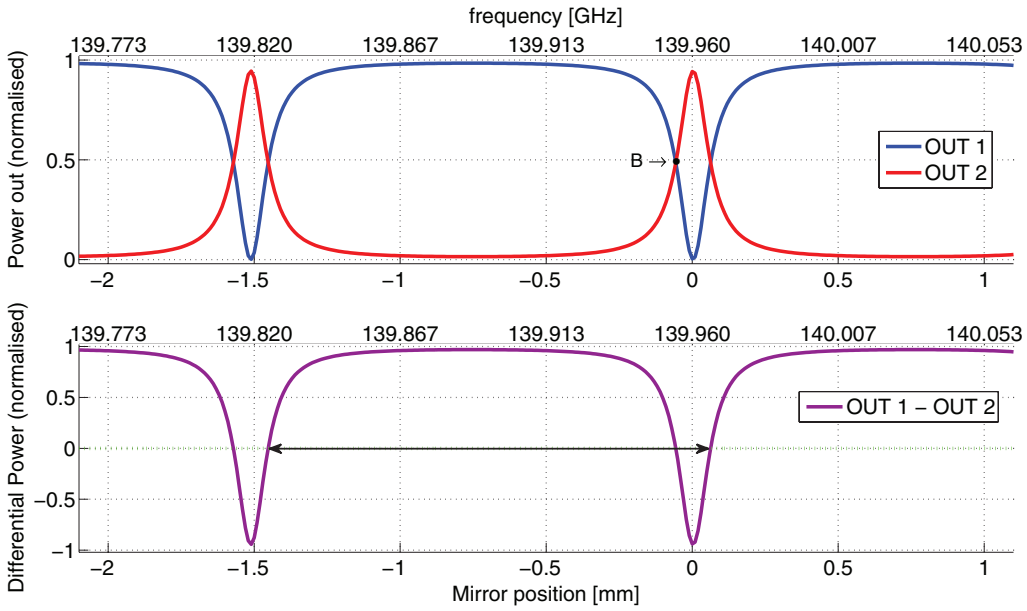

Figure 10. Diplexer power transmission curves as a function of frequency (with fixed L) and as a function of mirror position (with fixed f). Upper: output beams OUT1 and OUT2. Lower: the differential power of OUT1 and OUT2; the green line shows the desired value.

the latter case the relation between the controlled variable (i.e. the mirror position) and the error signal is *linear*. The relation between the controlled variable and the power-based error signal is clearly *non-linear*, as is also illustrated in the lower graph of figure 10. This is a result of the properties of OUT1 and OUT2 as a function of the mirror position. The power signals OUT1 and OUT2 have a non-linear gain relation with the mirror position, and they lack phase information (non-negative values) and are periodic with the wavelength λ (in the working area of the resonator). The error function e has similar periodicity, which means that several solutions exist for the mirror position that all render zero error (power equalization of OUT1 and OUT2). For each period of one λ two error minima exist. In practice, only one particular solution will be acceptable for fast switching, because of the specific frequency-shift keying of the gyrotron.

The control approach to handling the non-linear behavior of the power error function consists of: (1) an appropriate gain scheduling technique together with (2) a restriction on the operational range of the mirror position. The limitation on the mirror position implies that for a selected power equalization point B, the allowable range of mirror positions is bounded by the area between the two neighboring minima, equaling a total position range of $\lambda/\sqrt{2}$; for operation point B this is indicated by the black arrow in figure 10. Within this range, the controller is capable of driving the resonator to the desired error minimum. Outside this range it will drive the resonator to another—though undesired—error minimum. In order to have the mirror motion system reject undesired disturbances and at the same time ignore the fast frequency-shift keying of the gyrotron (as intended for switching), an analog low-pass filter with a cut-off at 5 kHz has been installed, to attenuate the fast fluctuations in the OUT1 and OUT2 power sensor signals. Note that mechanically induced switching (i.e. by vibrating the 15 kg mirror) is limited to the bandwidth of 100 Hz of the mirror control system.

4. NTM stabilization experiment using fast switching

4.1. Setup

The setup for these experiments uses similar target plasmas to those for modulation experiments without switching as described in section 2. The setup of the injection geometry is shown in figure 8 (left), and the ideal phasing for both launchers is shown in figure 4. For the experiments, the gyrotron output power (prior to modulation) was set to 490 kW; the relatively low value was used to avoid arcing in the diplexer resonator (note that the circulating power in the resonator is about a factor of 4 higher than the transmitted power). The cathode modulation voltage was set to 2.8 kV, to obtain on the one hand sufficient frequency modulation, and on the other hand a tolerable power loss due to the concomitant power modulation. The diplexer control was tuned to obtain similar power in both launchers. Details on the launched power and switching contrast achieved with a FADIS are discussed in the next section. The generation of the NTM had to be modified for the switching experiments since the total NBI power on the experimental days was limited to 7.5 MW due to hardware failure. Triggering of a (3,2)-NTM at this power level was achieved by changing to a low-density ramp-up with early heating as developed for the improved H-mode program [19]. As described in this reference, the q-profiles generated at the end of such a ramp-up facilitate the formation of small (3,2)-NTMs. After the NTM was triggered, the plasma fueling was increased to the levels of our previous stabilization experiments, in order to end up with similar q-profiles. In fact, the

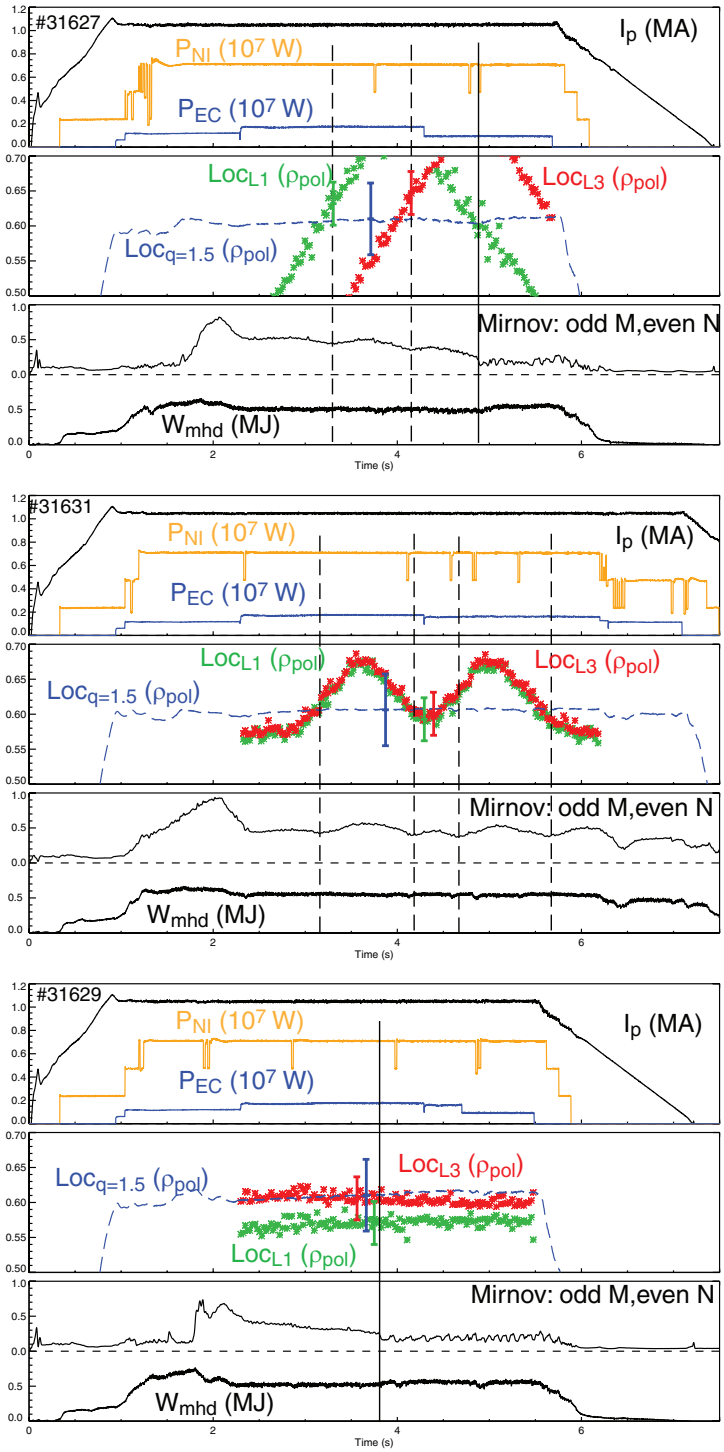

Figure 11. Three different discharges using a FADIS to switch the power of one gyrotron between L1 and L3. For each discharge several time traces are shown: the heating power of NBI and ECRH and the plasma current on top, in the middle the radial positions of the ECCD locations for L1 and L3 as calculated by RT-TORBEAM, and the position of the $q = 1.5$ surface from the RT-equilibrium (all in ρ_{pol}). The error bars indicate the maximum expected deviation of the real positions from the calculated ones, derived in [12] for the ECCD locations and in [20] for the position of the resonant surface. Shown below is the positive envelope of the odd *m*/even *n* Mirnov signal and the stored energy. For all three discharges dashed vertical lines indicate a minimum in the Mirnov amplitude related to the launcher movement, and solid lines indicate the stabilization of the NTM, which is a (3,2) in all cases. Note that the noise level for these signals lies between 0.1 and 0.2 (a.u.).

modes were finally observed at the same radial location with similar amplitude and frequency, indicating that the q-profiles were sufficiently close.

4.2. Results

Figure 11 shows the major results of the NTM-stabilization experiments using a FADIS.

First (top) we scanned both launchers with a large angle across the radial region where the NTM is expected using feedforward launcher control. The radial locations of the deposition were chosen to be radially out of phase such that the $q = 1.5$ surface is not crossed at the same time. This allows one to study the effect of each launcher separately. The figure compares the deposition location as calculated from RT-TORBEAM with the radial location of the $q = 1.5$ surface. Ideally, one expects the most significant effect on the mode amplitude when the ECCD location matches the $q = 1.5$ position. Indeed, the mode amplitude (Mirnov signal envelope) shows a minimum close to each crossing for both launchers. At the second crossing with L1 the mode is even stabilized. We ascribe this to the two successive arcs in one NBI source, which appeared when the launcher was crossing the $q = 1.5$ surface; thus, the driving term of the mode (β, W_{mhd}) was reduced just when ECCD was close to the $q = 1.5$ surface. Note that at the first crossing with L1 (with properly operating NBI), the mode was not stabilized. Therefore, we assume that one launcher is not sufficient for stabilization. Note that W_{mhd} rises significantly after NTM stabilization.

For the next step the aim was to demonstrate mode stabilization pointing both launchers at the $q = 1.5$ surface at the same time in order to stabilize the NTM without failure of the NBI system. Such an experiment adds additional complication since the ECCD locations come with offsets of the order $\pm 0.025\rho_{\mathrm{pol}}$ due to uncertainties of the equilibrium and the density profile [14, 21]. These offsets are unfortunately not constant and seem to depend on the stabilization strategy indicating a (small but significant) radial movement of the NTM as the ECCD deposition approaches. Comparing launchers above and below the mid-plane as L1 and L3 (figure 8) these offsets cannot be expected to be correlated (and therefore to cancel out in our application), since the beams probe different radial ranges of the density profile and different regions of the equilibrium. A vertical error of the latter would even introduce an anti-correlation, i.e. the worst case for our application. These issues are currently under study using non-modulated ECCD for NTM stabilization, but no well developed solution exists yet on ASDEX Upgrade, except to raise ECCD power. For our experiment we concluded from the first crossings with L1 and L3 in figure 11 (top) that both minima in the mode amplitude occurred at very similar reconstructed values of ρ_{pol}, such that we might get away with not compensating for different offsets. For launcher control we used pre-programmed ρ_{pol}, which the DCS realizes using RT-TORBEAM, and a model for the launcher drive (dead-times, default accelerations) [22]. Figure 11 (middle) shows the result. Although the nominal deposition locations lie well on top of each other, the NTM is not fully stabilized, but all four crossings come with a clear minimum in mode amplitude. One reason could be the finite time of the overlap between the mode and deposition region. Another possible explanation relates to uncertainties in the deposition as discussed before, and indicated in the figure by error bars. This interpretation is motivated by figure 11 (bottom), where we can get full stabilization within the uncertainties of the deposition location.

Fortunately, an experiment with long overlap was initiated by an unexpected failure of our mirror control, which delivered the necessary evidence for complete stabilization, as shown in figure 11 (bottom). Here the mirror positions were frozen early in the discharge. The variation in time calculated by RT-TORBEAM is only due to variations of the density profile and a slight current diffusion which affects the equilibrium. L3 is close to the nominal $q = 1.5$ surface, slightly crossing it as time evolves. In contrast to the discharges in figure 11 (top, middle), the mode amplitude slowly reduces as soon as the stabilizing gyrotron is switched on. At approximately 3.8 s the mode stabilizes. At this time point, L1 aims nominally $\Delta\rho \approx 0.03$ further inside. This clearly proves that we suffer from uncertainties in the mode location in the same range as those observed without modulation before, as we could get full stabilization within the uncertainties of the deposition location.

So we have strong indications that we can stabilize the NTM with ≈0.5 MW of ECCD applied 'almost continuously' (detailed discussion at the end of this section) close to the O-point by using switching with a FADIS. We also know that we did not manage to stabilize the NTM for the same conditions in an earlier attempt, in which an earlier version of the resonator control was not able to maintain the optimum operational point, and the switching contrast almost vanished [23]—i.e. we have shown that optimization of the switching contrast matters, as expected from the results of section 2.

The remaining open questions first require an optimization of the algorithm which sets the launchers. As mentioned above, the fine tuning of the beam position is the topic of ongoing experiments on AUG, either using the mode amplitude [21] or potentially the output of an in-line ECE system [24] for optimization. If one has confidence that an optimized launcher position can be routinely achieved, one can address issues like 'what is the minimum power needed to stabilize an NTM for a specific machine and its specific ECCD sources, for a specific beta, density profile and current profile given a certain switching contrast?' On ASDEX Upgrade, experiments to study such issues do not necessarily require fast switching between launchers, but these issues can be addressed using a (modulated) gyrotron per launcher. These questions are beyond the scope of this paper.

We end this section by addressing the accuracy of the locking of the ECCD to the O-points of the island. As a starting point, we refer to the discussion of this issue for the case without a FADIS at the end of section 2.4. A similar histogram approach shows that the power switching time for the 2.5 kV steps is 6 ± 1 μs (figure 12). In contrast to figure 7 the 'ears' of the histogram are significantly asymmetric and the maximum steps are larger for the rising edge than for the falling edge. A more detailed analysis shows that increasing voltage comes with a voltage overshot of 120 V, while decreasing voltage

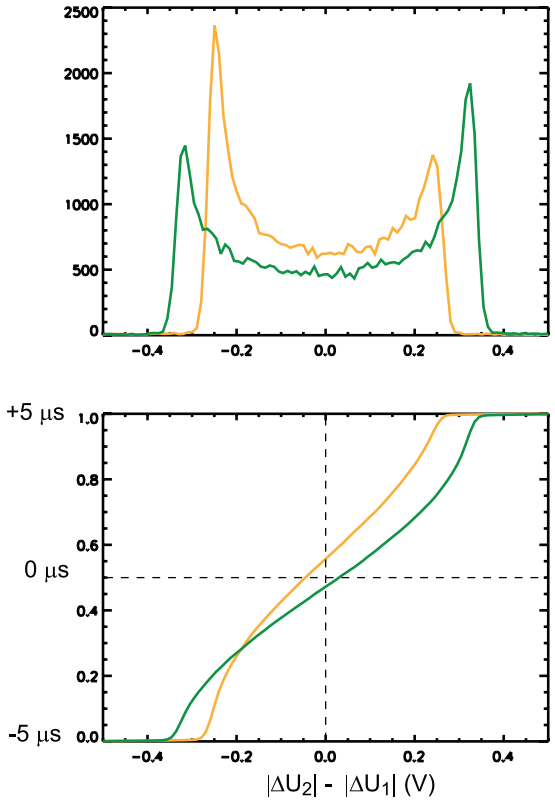

Figure 12. Histogram and its normalized integral similar to the right part of figure 7, but now for a reduced modulation depth of the cathode voltage (2.5 kV instead of 13 kV). This results in a smaller power modulation of the gyrotron and consequently the voltage variation at the directional coupler in M2 is much smaller. Green: rising edge; orange; falling edge. Shown are data for discharge 31 631 in the time interval from 2.8 s to 5.8 s (see figure 11 middle).

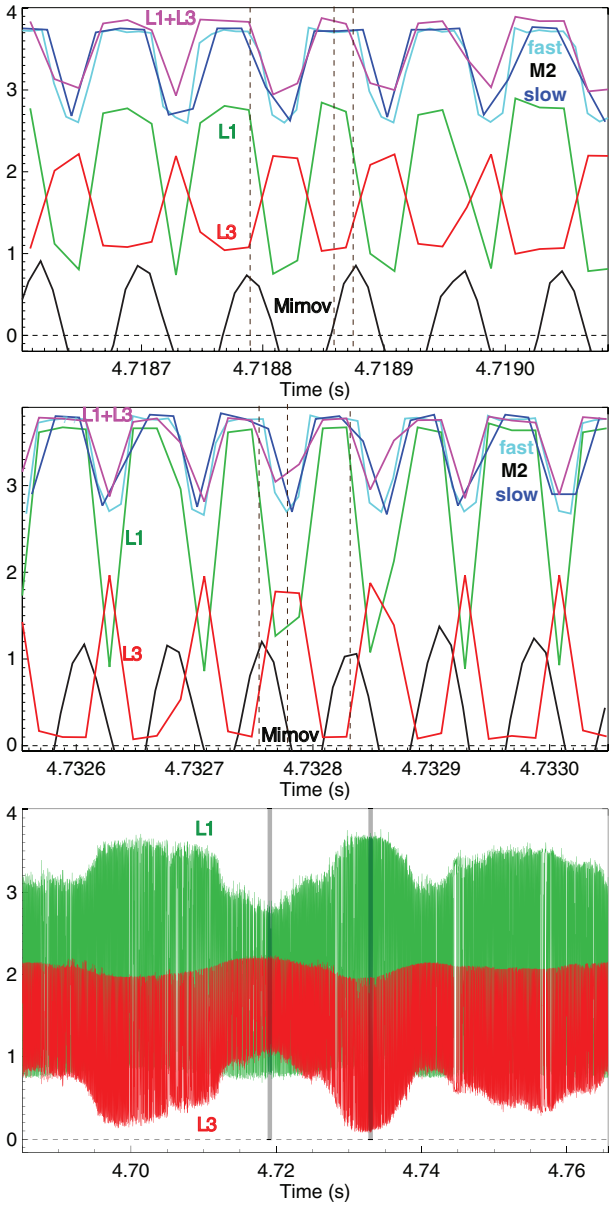

Figure 13. Timing of power through L1 (green) and L3 (red) relative to the odd-*m*, even-*n* Mirnov signal. Additionally shown is the launched power as determined by the directional coupler in M2 and corrected for transmission and diplexer loss (blue: old data acquisition; cyan: new data acquisition), as well as the sum of the green and red curves (magenta). All except the Mirnov signal are given in units of 100 kW. The top and middle show the cases for different operational points of the FADIS for discharge 31 627 (see also figure 11, top). Below, for the same discharge a longer time interval is shown (only L1 and L3), which allows one to locate the two different phases and shows that they correspond to two extremes of the resonator operation. The vertical bars in the upper two parts are used to determine the relative phasing of L1 and L3 with respect to the Mirnov signal.

tends to creep to its final value. Note that 100 V is the designed stability for the output voltage of the series modulator.

The easiest approach to determine the phases of the ECCD through L1 and L3 would be to assume that the central time of each higher-voltage plateau corresponds to a maximum of power through L1 and the central time of each lower-voltage plateau corresponds to a maximum of power through L3. In fact this will turn out to be a good assumption when the resonator control is operating well. This can be verified using additional signals from two miter bends located between the FADIS and the respective launchers, which are used as a measure for the transmitted power, and which give the input signals for the diplexer control. In our configuration these miter bends are located in the torus hall, and the data are sampled with a frequency of 50 kHz after being digitally transmitted via an optical fiber. The digital optical-fiber transmission comes with an *a priori* unknown delay of 10–20 μs. This old 50 kHz data acquisition is based on a local quartz oscillator in contrast to the new 100 kHz system which uses a central clock and is the basis for figures 7 and 12. In order to check the identity of the time bases of both data acquisition systems in the μs range, we split the gyrotron power signal (from mirror M2) on the FADIS entry side, and sample it with both data acquisition systems, in both cases without a transmission via optical fiber. This allows us to correct the timing of the old 50 kHz system with respect to the new 100 kHz system (offset-linear correction, $\Delta t_{\max} \approx 30$ μs). All three signals (from M2 and the two

Table 1. Available output power (kW) for the gyrotron (peak power, average power), average injected power at the launcher(s), and power deposited mainly in the O-point and X-point of the islands for the FADIS and the reference experiments.

Operation .	Gyr. P peak	Gyr. P av.	Plasma P inj.	O-point P	X-point P	Stabilization reached?
FADIS	490	431	354	316	38	yes
Power Mod.	780	455	410	350	60	yes
Power Mod.	780	455	410	60	350	No
CW	780	780	700	350	350	yes

miter bends) are voltages from diodes connected to directional couplers, which can be converted to incident power using calibration curves. For M2 a direct calibration from voltage to gyrotron power exists. The directional couplers in the miter bends are not yet calibrated (and calibration depends on the chosen polarization). Assuming that the FADIS operates almost loss-free, the M2 signal should be a linear combination of the two miter bend signals, if the (common) delay time due to the digital optical transmission is chosen correctly. Several 10 000 switching cycles allow us to set these quantities rather accurately. Here we do not use the full mathematical apparatus but after some trial and error we are confident to have determined the time delay to be 15 ± 3 μs and the calibration factors to be $\pm 10\%$. For our purpose this is sufficient, since at this stage we aim to get the phasing right within $\pm\pi/4$, which corresponds to ± 10 μs.

Figure 13 (top and middle) shows the results of such timing reconstructions for two different operational points of the FADIS. In the bottom part of the figure the time resolution is much coarser to show how the operational point varies in time as a consequence of the resonator control. For the rather rectangular power signals the limited time resolution of the data acquisition does not lead to artificial variations of the amplitude (there is always at least one point of each plateau sampled) in contrast to the expectation for a harmonic variation, but manifests itself in a variation of the widths only. The two operational points picked for the figure correspond to the extremal values reached for the resonator control. Using the indicated vertical lines in the figure the relative phasing between the odd-m, even-n Mirnov signal and L3 is determined as 2.02 rad in the upper case and 2.09 rad in the lower case which compares to the value of 2.2 rad for the optimum phasing from figure 4—about 10° off. Since the ideal phases for L1 and L3 are not perfectly opposed to each other, the error for L1 is ≈20°. We conclude that even if an error of several μs is assumed we have reached the goal to match the phases better than $\pi/4$.

From figure 13, the switching contrast K ($K = 1 - P_{\min}/P_{\max}$) for both launcher channels can also be obtained. For the resonant channel L1, $K \approx 0.73$ and is rather constant in time, as the operation point B is somewhat above parity. For L3, the finite accuracy in the mirror position control or gyrotron frequency of ± 30 μm or ± 3 MHz leads to variations of K between 0.53 and 0.95 during the shot—i.e. the average value is also around 0.74. From these data, an average frequency-shift keying of only 7 MHz is derived (taking the curves given in figure 10); this value, however, is significantly less than the frequency modulation of 10–12 MHz measured before at a modulation frequency of 200 Hz. Nevertheless, a sufficient switching contrast is obtained.

The average power, which is launched synchronously to the O-point from both L1 and L3, is estimated to be $P(O-\text{point}) = 279$ kW; for the average cw power on both launchers, we estimate $P(\text{CW}) = 75$ kW. Here, a gyrotron output power (without modulation) of 490 kW, a general transmission efficiency of 95%, a gyrotron power modulation of 24%, a loss for high-order modes in the resonant channel of 5%, and a diplexer insertion loss of 6% and 2% [16] for the resonant and non-resonant channels, respectively, were assumed.

Table 1 summarizes the power deposited in the O-point and X-points with the diplexer and gives a comparison with the power injected in the reference experiments.

5. Summary and outlook

5.1. Summary

The present FADIS experiments on ASDEX Upgrade with the diplexer Mk IIa have clearly demonstrated that efficient NTM stabilization is possible via fast switching of the ECCD power between two launchers, synchronous to the rotating islands of the 3/2 NTM. For this demonstration experiment, many ingredients were required: The Mk II diplexer had to be integrated into a pair of transmission lines, which were connected to a top and a bottom launcher of the ECRH-2 system. Careful preparation of the experiment was mandatory. In particular, the magnetic field and the aiming of the launchers had to be controlled thoroughly for optimum power deposition in the islands. The signals from the Mirnov coils had to be processed via many steps to give a reliable signal for the phase-correct 2.8 kV voltage modulation of the gyrotron, resulting in a synchronous frequency-shift keying of 6–10 MHz. An optimum switching contrast was obtained by the fast control of a resonator mirror of the diplexer, compensating thermal and gyrotron frequency drifts. Thus, a switching contrast of typically 74% was reached, and complete NTM stabilization could be obtained with a launched power of below 400 kW using O-point deposition, while with X-point deposition, no stabilization resulted.

If one just takes this experimental result—with all its limitations—and the findings from the experiments without a FADIS, one can conclude that the required ‘installed gyrotron power’ for complete NTM stabilization with a FADIS was lower by a factor of about 1.6, compared to the CW and modulation reference experiments. Notably, due to the higher stabilization efficiency for O-point modulation compared to

X-point modulation and CW operation, we assume a ratio $w_{CD}/w_{marg} > 1$ for the diplexer experiments as well.

It should be noted that the present FADIS experiment on ASDEX Upgrade clearly is a proof-of-principle experiment, which for various reasons is not optimized for a quantitative analysis of the minimum power required for NTM stabilization: as the AUG ECRH employs only one launcher per gyrotron, a switching experiment between two launchers disables the operation of one gyrotron. Moreover, the power through Mk II is limited by arcing to about 500 kW, as it operates at atmospheric pressure. (Note that a transmitted power of 500 kW corresponds to about 2 MW in the diplexer resonator, if operated at point A). In addition, for correct FADIS operation, permanent control of the diplexer is required. For ASDEX Upgrade, this means that NTM experiments with synchronous power modulation of one gyrotron are much simpler and equally effective, as was shown in the paper. Further diplexer experiments at ASDEX Upgrade, therefore, will aim at in-line ECE to explore the possibilities of launcher control [25]. These should also allow a precise assessment of the power requirements for the different schemes.

5.2. Outlook: options for applications in large-scale ECRH systems

This paper demonstrates the FADIS application of resonant diplexers, which is only one feature of these devices. In future high-performance ECRH systems, where dedicated launchers are used for basic heating and current drive applications on the one hand, and for mode stabilization on the other, diplexers could play a central role in the DCS. Some aspects as well as integration concepts for various diplexer types are discussed in [26]. In this case, non-resonant outputs would be connected to standard launchers, and resonant outputs would feed dedicated launchers for mode stabilization. Thus, according to the physical needs, the EC power could be arbitrarily distributed between launcher pairs by simply tuning the diplexer resonance frequency, while the gyrotrons run continuously.

Therefore, when NTM stabilization is necessary, the required power is immediately available at the NTM launchers, without the usual delay of typically 2 s caused by the switch-off of the gyrotrons during the movement of the miter bend switches. When the effective diameters of the stabilizing beams are larger than the typical island sizes, e.g. by imperfect (mutual) alignment of the NTM beams, broadening of the beams by fluctuations, plasma parameters, and deposition radii [7], synchronous EC power deposition in the O-point is needed. Then, a relatively small gyrotron voltage modulation synchronous to the rotation frequency of the islands together with proper tuning of the diplexer will yield a strong amplitude modulation in the resonant diplexer output, i.e. at the NTM launcher, and thus yield high stabilization efficiency. The remaining (modulated) power at the other diplexer output, i.e. the standard launcher, is used to continue the ECRH application as before. The isolated input port of the diplexer can be used to receive ECE radiation from the plasma by sharing the NTM launchers with the (forward) ECRH [27]. After appropriate processing, the in-line ECE signal can be implemented into the control system of the experiment to steer the launchers for optimum deposition of the power in the NTM islands [28]. This port is also available for using the connected launcher for any microwave diagnostics operating around the EC frequency.

Resonant diplexers are also beneficial for the reliable operation of the ECRH system. The mode purification characteristics of the resonator [29] can improve the focusing and reduce the possible beam squint of NTM beams, as low-order spurious (i.e. undesired) modes in the waveguides distorting the launched beam pattern predominantly exit the diplexer at the non-resonant output port. Very-high-order modes are absorbed in the (absorber-loaded) resonator casing; this filtering reduces the thermal loading of the sensitive cuffs of the vacuum windows in the transmission lines as well as in the launcher components [30]. A stray radiation detector in the diplexer can serve as a monitor for mode purity. Eventually, if an upgrade of the ECRH power is needed, the second input ports of the diplexers could be used to connect further gyrotrons, as the diplexer can operate as a power combiner [16].

Naturally, the integration of diplexers in ECRH plants increases system complexity. Depending on the type, diplexers need space for installation, and for when they replace the mechanical waveguide switches routing the power between launchers. Evacuated transmission lines are mandatory to avoid arcing in the diplexer resonator. Additional insertion loss for the main HE_{11} mode must be taken into account: for a typical design of a resonant diplexer, the HE_{11}-loss in the non-resonant path is about 1% ; the HE_{11}-loss at the resonant output is about 4% [30]. This loss needs to be cooled from the mirrors and the internal stray radiation absorbers; cooling concepts for the mirrors are available from developments for ITER and W7-X [31]. In addition, very-high-order spurious modes will be absorbed in the diplexer as well, and have to be considered in the cooling capacity. Note that low-order spurious modes are not absorbed, but are transmitted mostly to the non-resonant output. Diplexers have some cross-talk (typically 2%; see figure 2, right) between output ports, which may need extra measures once a launcher channel is out of order. Control of the diplexer needs to be accounted for as well, including the processing of controlling and timing signals, as was described before. Note that other diplexer types [32] may have less loss or need less space for integration, but their scope of application is limited compared with ring resonator devices.

When accepting the extra technical effort concomitant with the use of diplexers, a universal EC power management system can be created, which in principle is adapted to the *in situ* control of ECRH and ECCD in the experiment. A possible use in ITER by replacing (part of) the waveguide switches in the junctions between the upper and equatorial launchers is subject to a detailed assessment with careful balancing of the advantages versus the implications and design changes of the well advanced ITER ECRH system.

Acknowledgment

Common development work and many discussions with M. Petelin, V. Erckmann, D. Shchegolkov, L. Lubyako, Y. Koshurinov, E. Koposova, H. Hoehnle, C. Lechte, P. Brand,

E. Filipovic, M. Saliba, F. Hollmann, F. Noke, F. Purps, A. Bruschi, W. Bongers, K. Sakamoto, M. Henderson, F. Gandini, R. van den Braber, M. de Baar, H. van den Brand, E. Westerhof and many others are gratefully acknowledged. We thank the mechanical and electronic workshops at IGVP Stuttgart for excellent work.

References

[1] Zohm H. 2015 *Magnetohydrodynamic Stability of Tokamaks* (New York: Wiley) ISBN 978-3-527-41232-7
[2] Maraschek M. *et al* 2007 Enhancement of the stabilization efficiency of a neoclassical magnetic island by modulated electron cyclotron current drive in the ASDEX Upgrade tokamak *Phys. Rev. Lett.* **98** 025005
[3] Isayama A. *et al* 2009 Neoclassical tearing mode control using electron cyclotron current drive and magnetic island evolution in JT-60U *Nucl. Fusion* **49** 055006
[4] Maraschek M. 2012 Control of neoclassical tearing modes *Nucl. Fusion* **52** 074007
[5] Kolemen E. *et al* 2014 State-of-the-art neoclassical tearing mode control in DIII-D using real-time steerable electron cyclotron current drive launchers *Nucl. Fusion* **54** 073020
[6] Henderson M.A. *et al* 2008 Overview of the ITER EC upper launcher *Nucl. Fusion* **48** 054013
[7] Poli E. *et al* 2015 On recent results in the modelling of neoclassical-tearing-mode stabilization via electron cyclotron current drive and their impact on the design of the upper EC launcher for ITER *Nucl. Fusion* **55** 013023
[8] Sauter O., Henderson M.A., Ramponi G., Zohm H. and Zucca C. 2010 On the requirements to control neoclassical tearing modes in burning plasmas *Plasma Phys. Control. Fusion* **52** 025002
[9] Petelin M.I. 2003 Quasi-optics in high-power millimeter-wave systems *AIP Conf. Proc.* **691** 251–62
[10] Kasparek W. *et al* 2008 A fast switch, combiner and narrow-band filter for high-power millimetre wave beams *Nucl. Fusion* **48** 054010
[11] Gruber O. *et al* and ASDEX Upgrade Team 2009 Compatibility of ITER scenarios with full tungsten wall in ASDEX Upgrade *Nucl. Fusion* **49** 115014
[12] Reich M. *et al* and ASDEX Upgrade team 2015 Real-time control of NTMs using ECCD at ASDEX Upgrade PPC/P1-26, paper presented at *25th IAEA Conf. on Fusion Energy (St. Petersburg, 2014)*
[13] Meskat J.P. *et al* 2001 Analysis of the structure of neoclassical tearing modes in ASDEX Upgrade *Plasma Phys. Control. Fusion* **43** 1325
[14] Reich M. *et al* 2015 Real-time beam tracing for deposition control of electron cyclotron wave heating *Fusion Eng. Des.* **100** 73–80
[15] Giannone L. *et al* 2013 A data acquisition system for real-time magnetic equilibrium reconstruction on ASDEX Upgrade and its application to NTM stabilization experiments *Fusion Eng. Des.* **88** 3299–311
[16] Kasparek W. *et al* 2011 High-power performance of a resonant diplexer for advanced ECRH *Fusion Sci. Technol.* **59** 729–41
[17] Wagner D. *et al* 2007 The new multifrequency electron cyclotron resonance heating system for ASDEX Upgrade *Fusion Sci. Technol.* **52** 313–20
[18] Doelman N. 2012 Controlled mirror motion system for resonant diplexers in ECRH applications *EPJ Web Conf.* **32** 04005
[19] Stober J. *et al* 2007 The role of the current profile in the improved H-mode scenario in ASDEX Upgrade *Nucl. Fusion* **47** 728–37
[20] Giannone L. *et al* 2015 Improvements for real-time magnetic equilibrium reconstruction on ASDEX Upgrade *Fusion Eng. Des.* **100** 519–24
[21] Rapson C. *et al* 2014 Amplitude based feedback control for NTM stabilisation at ASDEX Upgrade *Fusion Eng. Des.* **89** 568–71
[22] Rapson C. *et al* 2013 Simulation of feedback control system for NTM stabilisation in ASDEX Upgrade *Fusion Eng. Des.* **88** 1137–40
[23] Kasparek W. *et al* 2015 Development of resonant diplexers for high-power ECRH status, applications, plans *EPJ Web Conf.* **87** 04010
[24] Bongers W.A. *et al* 2012 Commissioning of inline ECE system within waveguide based ECRH transmission systems on ASDEX Upgrade *EPJ Web Conf.* **32** 03006
[25] van den Brand H. *et al* 2016 Inline ECE measurements for NTM control on ASDEX Upgrade *Nucl. Fusion* submitted
[26] Bruschi A. *et al* 2010 Diplexers for power combination and switching in high-power ECRH systems *IEEE Trans. Plasma Sci.* **38** 1427–38
[27] Hennen B.A. *et al* 2009 A closed-loop control system for stabilization of MHD events on TEXTOR *Fusion Eng. Des.* **84** 928–34
[28] van den Brand H., de Baar M.R., Lopes Cardozo N.J. and Westerhof E. 2012 ECE for NTM control on ITER *EPJ Web Conf.* **32** 03004
[29] Wu Z., Kasparek W. and Plaum B. 2015 Design and characterisation of a 170 GHz resonant diplexer for high-power ECRH systems *IEEE Trans. Microw. Theory Tech.* **63** 3537–46
[30] Kasparek W. *et al* 2012 Status of resonant diplexer development for high-power ECRH applications *EPJ Web Conf.* **32** 04008
[31] Hailer H. *et al* 2003 Mirror development for the 140 GHz ECRH system of the stellarator W7-X *Fusion Eng. Des.* **66–8** 639–44
[32] Kasparek W. *et al* 2009 High-power microwave diplexers for advanced ECRH systems *Fusion Eng. Des.* **84** 1002–5